**AUTHOR(S):** JAFARIFAR, N., PILAKOUTAS, K. and BENNETT, T.

**TITLE:** The effect of shrinkage cracks on the load bearing capacity of steel-fibre-reinforced roller-compacted-concrete pavements.

**YEAR:** 2015

**Publisher citation:** JAFARIFAR, N., PILAKOUTAS, K. and BENNETT, T. 2015. The effect of shrinkage cracks on the load bearing capacity of steel-fibre-reinforced roller-compacted-concrete pavements. Materials and structues [online], 49(6), pages 2329-2347. Available from: https://dx.doi.org/10.1617/s11527-015-0652-0

**OpenAIR citation:** JAFARIFAR, N., PILAKOUTAS, K. and BENNETT, T. 2015. The effect of shrinkage cracks on the load bearing capacity of steel-fibre-reinforced roller-compacted-concrete pavements. Materials and structues, 49(6), pages 2329-2347. Held on OpenAIR [online]. Available from: https://openair.rgu.ac.uk

# The effect of shrinkage cracks on the load bearing capacity of steel-fibre-reinforced roller-compacted-concrete pavements

Naeimeh Jafarifar[1], Kypros Pilakoutas[2], Terry Bennett[3]

[1, 2]*Department of Civil and Structural Engineering, University of Sheffield, Sir Frederick Mappin Building, Mappin Street, Sheffield, S1 3JD, UK*

[3] *School of Civil, Environmental and Mining Engineering, University of Adelaide, Engineering North N136, North Terrace Campus, SA 5005, Australia*

[1] Tel.: +44 (0)114 222 5729

[1] n.jafarifar@sheffield.ac.uk

## Abstract

This paper demonstrates the effect of shrinkage cracks on the static load bearing capacity and on the fatigue performance of RCC pavements reinforced with steel fibres recycled from post-consumer tyres, with the aid of a case study. A numerical method is adopted using material properties (moisture transport, free shrinkage, mechanical and fatigue) derived from experiments. It is shown that surface micro-cracks initially develop predominantly due to differential shrinkage (curling). These micro-cracks penetrate down to approximately a quarter of the slab thickness and it is shown that they reduce the ultimate load bearing and fatigue capacity of the pavement by up to 50%. Even though shrinkage does not initially induce visible cracks, it significantly intensifies the crack opening due to traffic load by up to 500% for a crack width of 0.5 mm. For the case studied herein, to assure the long-term performance of the pavement the allowable stress ratio should be reduced by half, to account for the effect of shrinkage distress. This study is useful because for the first time the mechanical characteristics are coupled with the moisture transport mechanism, as well as the shrinkage and fatigue characteristics. This methodology can be used for other similar materials and geometries and can lead to general conclusions regarding the importance of shrinkage distress on the design of pavements.

*Keywords: Shrinkage; SFRC; RCC Pavement; Numerical Analysis; Recycled Steel Fiber; Fatigue.*

## 1 Introduction

Modern road pavements are designed for a service life of 40 years or more, particularly for highly trafficked roads. Rigid concrete pavements normally have a longer life with less maintenance requirements than flexible asphalt pavements (Embacher and Snyder 2001). The cost of reinforced concrete pavements can be higher than that of asphalt pavements, especially due to the cost of reinforcement and joints; lower-cost reinforcement (such as steel fibres recycled from post-consumer tyres (UoS 2005)) could be utilised to further reduce the costs. Steel fibres can replace the commonly used steel fabric mesh and are added to wet concrete to facilitate construction and reduce labour costs as well as construction time. For even faster construction, roller compacted concrete (RCC) technology has been proposed for use with steel fibre reinforced concrete (SFRC). Ecolanes (2006-2009), an EU funded research project, developed optimised processes for roller-compacted SFRC (SFR-RCC) to produce long lasting pavement infrastructure for surface transport, utilising recycled-tyre-steel-fibres (RTSF) (Neocleous et al. 2006; Achilleos et al. 2011; Neocleous et al. 2011; Graeff et al. 2012; Jafarifar 2012; Jafarifar et al. 2014).

As pavements generally have a large surface area, shrinkage-induced cracking in concrete pavements is more critical than in other structural members (Zhang and Li 2001) and can significantly affect their performance and lifetime (Nam et al. 2006; Kwon and Shah 2008). Curling resulting from drying shrinkage is a common cause of pavement slab failure (Ruiz et al. 2005) and creates high stress regions near the drying surface (Lee et al. 2010). Curling also affects the support conditions under the pavement (Ruiz et al. 2005; Lee et al. 2010), and when combined with traffic load, increases the stress levels in the slab thus accelerates cumulative damage in the pavement (Jiang and Tayabji 1998; Ruiz et al. 2005).

The use of steel fibres in concrete pavements is beneficial in reducing the adverse effects of shrinkage by controlling shrinkage strain distribution and crack growth (ACI 544.1R 1996). Design guidelines specifically developed for SFRC are normally aimed at industrial ground slabs (e.g. Concrete Society TR34 2003). However, early-age distress, its interaction with service loads and long-term behaviour of pavements are not directly addressed by these guidelines.

The objective of this paper is to quantify distress induced by drying shrinkage in SFRC pavements (particularly RCC reinforced with RTSF), and its consequent effect on the long-term load bearing capacity. A thorough methodology is developed to take into account shrinkage in the design of SFRC pavements for long-term performance. Although the study focuses on a specific type of concrete pavement and utilises typical environmental and boundary conditions, the methodology can be used for other concrete types, slab geometries and boundary conditions.

The paper begins by presenting experimental studies followed by data processing to obtain the material characteristics, by numerical inverse analysis. The factors involved in moisture transport and drying shrinkage of concrete pavements are then reviewed and the relevant material properties are discussed, including how they are determined. A typical RTSF-reinforced RCC (R-SFR-RCC) pavement is then analysed for restrained shrinkage.

The analysis finally couples shrinkage distress with load bearing capacity and long-term fatigue performance before arriving at conclusions.

# 2 Material properties of SFRC

Experimental studies were necessary to obtain the mechanical properties needed for computational modelling. This section presents experimental studies and data processing to obtain post-cracking strain softening (σ-ε) behaviour, as well as moisture transport and shrinkage properties of the studied SFRC.

## 2.1 Experimental studies and results

### *2.1.1 Mix proportions and characteristics*

The R-SFR-RCC mix was cast using graded crushed granite typically utilised in the UK. The cement used in the study was a sulfo-aluminate low energy cement, since the aim of Ecolanes was also to reduce the energy demand during construction. The mix proportioning was based on typical mixes for road pavements in the UK (R-SFR-RCC: cement 300 kg/m$^3$; W/C 0.54; crushed aggregate 2084 kg/m$^3$). The nominal maximum size of coarse aggregates was limited to 14 mm, which also helps to avoid balling and to optimise the amount of recycled fibres in concrete. The gradation of the aggregates is given by Jafarifar et al. (2014). The water content was chosen to yield the maximum dry density of the compacted mix; 7% gave the highest dry density for the used cement and aggregates.

The fibre content was the optimum practical amount for RTSF determined by the Ecolanes project (60 kg per each cubic meter of concrete or around 2.5% by mass). RTSF have irregular shapes and lengths so their length distribution is determined using optical measurements (Neocleous et al. 2011). The average diameter of these fibres was 0.1-0.23 mm. In this study 85% of the fibres had length in the range of 10-25 mm, and 50% of them in the optimum range of 15-25 mm. The statistical length distribution of fibres and the casting method is presented by Jafarifar et al. (2014).

The mean compressive strength of the mix at 28 days was 51 MPa, obtained from 3 cube specimens, with a standard deviation of 1.0 MPa. The long-term (90 days) compressive strength was 56 MPa, obtained from 3 cylinders 150 ×300 mm with a standard deviation of 3.9 MPa, based on BS EN 12390-3 (2009).

### *2.1.2 Bending tests*

To determine flexural toughness, bending tests were performed on 150 ×150 × 550 mm beams adopting a four-point load arrangement at 150 mm centres. The specimens were cast in steel-plate moulds following the recommendations of BS EN 14651 (2005), and cured for 90 days in water, prior to testing. Long-term curing was performed to obtain the mature properties of concrete required for studying its long-term performance.

Some references (BS EN 14651 (2005) and RILEM TC 162 TDF (2002)) recommend to make a notch at the middle of the beam in order to concentrate cracking, whereas some others (ASTM C 1018 (1997) and JCI-S-003 (2007)) do not necessitate a notch. In this study 3 notched and 1 un-notched specimens were tested for comparison. Notches were cut (25 mm height and 5 mm width) on one side of the specimens mid-span and perpendicular to the compacted layers, using a rotating diamond blade. The specimens were tested in a servo-hydraulic universal testing machine under displacement control at a constant rate of 0.2 mm/min.

Mid-span beam deflections versus applied loads are shown in Fig. 1. From the bending test results, the average elastic modulus of the concrete was found to be 41 GPa with a standard deviation of 1.6 GPa. These results are used in Section 2.2 to determine the material stress-strain characteristics.

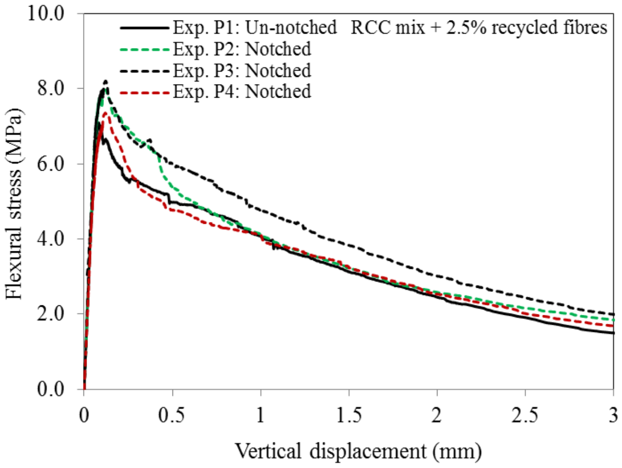

**Fig 1** Experimental bending test results

### 2.1.3 *Drying and shrinkage tests*

To determine the moisture transport properties of the concrete, drying tests were performed on 180×150×150 mm long prisms using a gravimetric method. Preparation of the specimens and the gravimetric method used for moisture measurement are presented in detail by the authors in Jafarifar et al. (2014). Moisture measurement was performed in an environmental chamber with relative humidity of 40±3% and temperature of 25±3ºC. Fig. 2(a) shows the time history of moisture profiles as the mean value taken from three specimens for each depth; this results can be used to back-calculate the moisture diffusivity and the surface factor (explained in Section 2.3).

Free shrinkage tests were performed on prismatic 150 ×150 × 550 mm specimens. To eliminate the effect of boundary conditions on fibre distribution and due to limitations in compacting RCC in small moulds, this specimen size is bigger than what is normally used for conventional concrete (ASTM C 157 (2008); BS EN 12617-4 (2000)). The environmental conditions were the same as those for the specimens in moisture measurement. To provide unrestrained conditions, the specimens were rested on two sharp edges and the length changes were measured over time, using a specially developed Vernier type device with an accuracy of ±0.02 mm (for more details refer to Jafarifar et al. (2014)). Fig. 2(b) shows free shrinkage strain versus drying time, as the mean value taken from three specimens; these results can be used to back-calculate the hygral contraction coefficient (explained in Section 2.3).

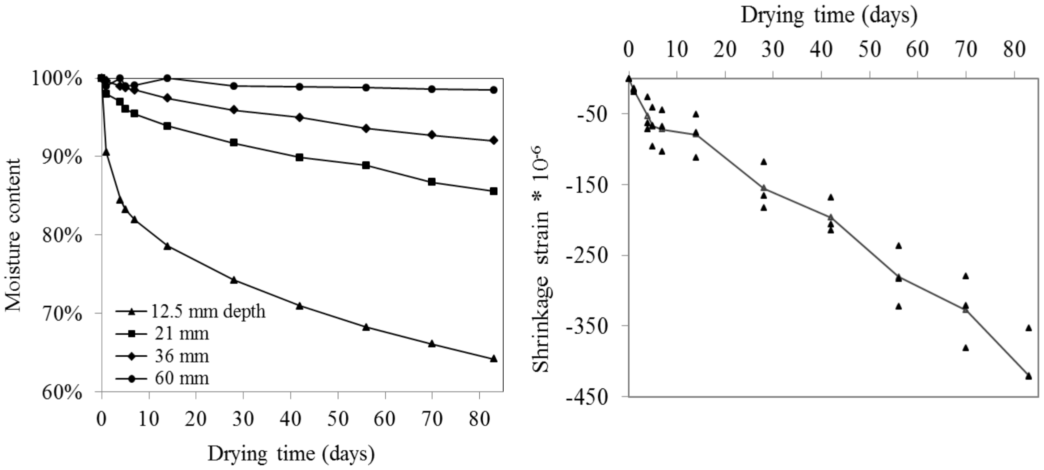

**Fig 2** (a) Experimental moisture profiles; (b) Experimental free shrinkage

## 2.2 Data processing to obtain post-cracking strain softening diagram (σ-ε)

The post-cracking σ-ε relationship can be obtained from the bending test results using inverse analysis; the path of the σ-ε curve is iteratively chosen so that the numerical $P-\delta$ curve matches the experimental one. In this paper for cross checking purposes, both section analysis and the FEA method are used for this purpose.

Section analysis is an iterative procedure to calculate the stress distribution through an individual cross-section. In this method, the key assumption is that plane sections remain plane. The stress distribution through the mid span cross-section is calculated based on force equilibrium, and the neutral axis depth is iteratively modified at each load step. Moment versus curvature of the section is transformed into load versus mid span deflection, using classical equations (Casanova and Rossi 1997). The multilinear σ-ε relationship back-calculated from sectional analysis is shown in Fig. 3(a), and the $P-\delta$ curves predicted based on this relationship is shown in Fig. 3(b) for the notched and unnotched prisms in comparison with the experimental results. The objective of the sectional inverse analysis is to minimize the error between experiments and prediction to less than 2% (in average) so as to eliminate the possibility of multiple σ-ε solutions.

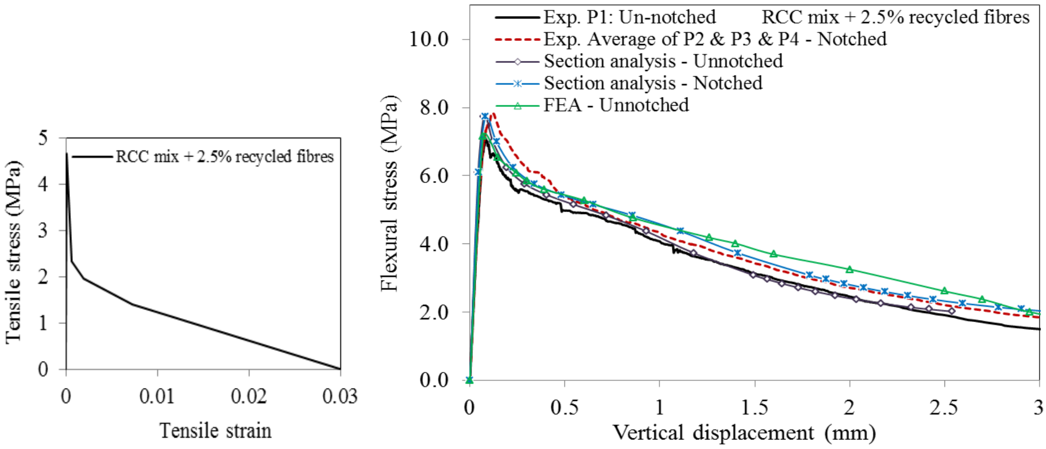

(a) (b)

**Fig 3** (a) Back-calculated σ-ε relationship, from inverse analysis; (b) Load-deflection curves predicted by section analysis and FEA, based on the assumed σ-ε relationship, compared with the experimental values

In the FEA method, the smeared crack approach has been used via “Concrete Damage Plasticity” material model in the finite element package ABAQUS (2010) and the results are shown in Fig. 3(b) based on the σ-ε relationship obtained from section analysis. The excellent correlations confirm that the back-calculated σ-ε relationship is objective and reliable.

## 2.3 Moisture transport and shrinkage properties

Moisture movement in drying concrete is a key parameter needed to predict shrinkage (Kodikara and Chakrabarti 2005; Sakata 1983). When drying occurs, the pore water moves towards the surface and results in variable moisture content in space and time. The flow of moisture in drying concrete is in general assumed to obey the diffusion theory (Pickett 1946; Bazant and Najjar 1972; Sakata 1983; Asad et al. 1997; Rahman et al. 1999; Kodikara and Chakrabarti 2005). This assumption works well especially when the moisture content decreases below 70-80% of initial full saturation (Selih et al. 1996). The diffusion equation describing moisture movement in concrete is similar to the equation of heat conduction, though the order of magnitude of the corresponding coefficients is entirely different (Pickett 1946). Hence, the transport of moisture in concrete can be characterised by Fick’s second law (Asad et al. 1997; Rahman et al. 1999).

To model drying shrinkage in concrete these material properties need to be determined:

(1) diffusion coefficient, $K_C$; (2) convective moisture transfer coefficient (also called surface or film factor), $f$; (3) the relationship between moisture loss and free shrinkage strain (Hygral contraction coefficient), $\beta_C$(C). To determine these, numerical inverse analysis can be used when moisture measurements and shrinkage tests are available. The numerical procedures to obtain these properties from the experimental data for the studied SFRC mix are presented in detail by the authors in Jafarifar et al. (2014). From that study, the moisture diffusivity, $K_C(C)$, was obtained as a function of moisture content, $C$, as shown in Fig. 4(a); It varies in the range of 0-5 mm$^2$/day for moisture content lower than 88% and then increases sharply. The surface factor was found to be around 5 mm/day, and the variation of $\beta_C(C)$ versus moisture content, $C$, is presented in Fig. 4(b). The hygral contraction coefficient of SFRC is generally lower than that of plain mixes due to the restraining effect of the fibres and the different pore structure of SFRC (Jafarifar et al. 2014).

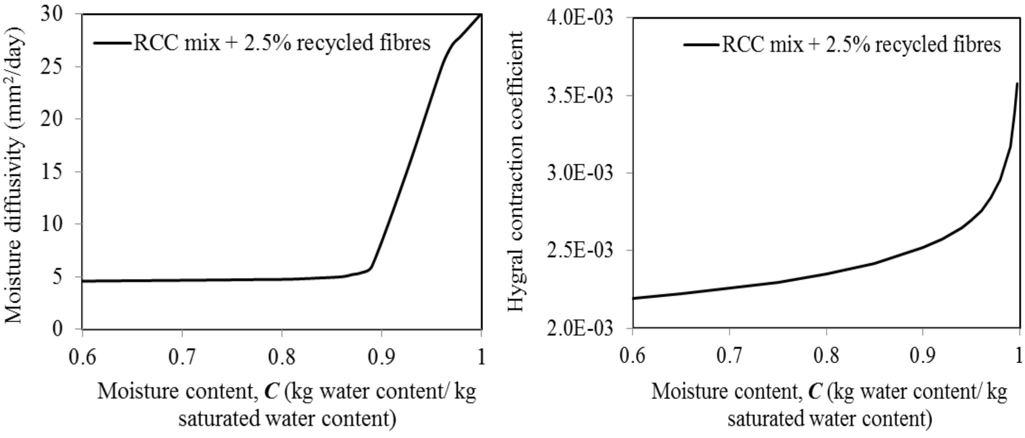

(a) (b)

**Fig 4** (a) Moisture diffusivity, $K_C(C)$, versus moisture content; (b) Hygral contraction coefficient, $\beta_C(C)$, versus moisture content (Jafarifar et al. 2014)

The hygral contraction coefficient, $\beta_C(C)$, can be used to predict free shrinkage strain, $(\varepsilon_{sh})_C$, as a function of moisture content, using Eq. 1.

$$\left(\varepsilon_{sh}\right)_C = -\beta_C(C) \times (C_0 - C) \qquad \text{(Eq. 1)}$$

Where, $C_0$ is the reference moisture content, set equal to 1.0 for initial saturation.

# 3 Numerical study of a typical road pavement for restrained shrinkage and monotonic loading

This section uses finite element analysis (FEA) to examine the effect of drying shrinkage on the short-term behaviour of a typical R-SFR-RCC pavement. The smeared crack modelling approach is adopted as it does not need a-priori knowledge of the cracking pattern. In ABAQUS, smeared cracks can be modeled using the “Concrete Damage

Plasticity” constitutive material model. This constitutive model uses the concept of isotropic damage in combination with tensile and compressive plasticity to define the inelastic behaviour of concrete. In tensile zones, inelastic deformations represent crack opening smeared over the element length. The direction of the maximum principal plastic strains can also be viewed as the normal vectors of the cracked planes (ABAQUS 2010).

The data required for this model are:

(1) Uniaxial tensile strain softening ($\sigma$-$\varepsilon$), obtained experimentally (see Fig. 3(a)).
(2) Uniaxial compressive strength, obtained experimentally (Section 2.1.1).
(3) Damage factors in tension as defined in ABAQUS (2010); in the absence of experimental values, these factors can be applied at the same rate as tensile strain softening.
(4) Damage factors in compression as defined in ABAQUS (2010); compressive damage is applicable for compressive strain-softening regime, which will never be reached herein since the compressive stresses are not dominant.
(5) Multi-axial yield and flow parameters including dilation angle, $\psi$ (the best value from surveying literature is 31°); eccentricity, $\varepsilon$ (a typical value of 0.1 is used); the ratio of biaxial compressive strength to uniaxial compressive strength (a typical value of 1.2 is used for SFRC); and *Kc* ratio as defined in ABAQUS (2010) (ranging from 0.5 to 1.0 with the default value of 2/3 adopted in this study).

The pavement was analysed using a 3D model which simulates the concrete slab on a multi-layered foundation, as illustrated in Fig. 5(a). The modelling assumptions are described in Section 3.1. Moisture transport analysis is first carried out and spatial moisture profiles are calculated as functions of time. In Section 3.2 moisture transport analysis is coupled with structural analysis. The time history of shrinkage strains is used to assess stresses and predict crack development at the pre-loading stage. Finally, in Section 3.3, the slab is analysed for structural (wheel) loads and the performance of the slab is discussed.

## 3.1 Model details and assumptions

### *3.1.1 Service load*

Based on the commonly used historical approach, traffic load (from wheel loads of various magnitudes, configurations and repetitions) is converted to an equivalent number of standard axle loads (SAL) to simulate overall damage expected on pavements. In this paper, the SAL of 80 kN (single axle with dual tyres) is adopted with a service life of 300 million standard axles (msa), as specified for design purposes in the UK (Hassan et al.

2005). The footprint of each tyre is taken as a rectangle of size 240 × 120 mm, with a distance of 240 mm between tyres at each side and a track width of 2.4 m.

### 3.1.2 Geometry

A lane width of 3.4 m and a slab thickness of 200 mm is chosen based on the design criteria proposed in Highway Agency report TRL630 (Hassan et al. 2005). The length of the slab is modelled long enough (three times the width) to account for the continuity of the pavement, and a continuity constraint is applied to one end (see Fig. 5(a)).

### 3.1.3 Foundation

As shown in Fig. 5(a), the foundation comprises the original subgrade soil, a layer of ballast as the granular subbase, and a layer of cement bound material; the latter being highly recommended for rigid pavements as base (Rogers 2003; Hassan et al. 2005).

In the design of concrete pavements, the stiffness of the foundation is mainly characterised by a k-value, modulus of subgrade reaction (NCHRP Report 372 1995). This approach assumes that the foundation deflects under an applied vertical force in direct proportion to the force without shear transmission to adjacent areas. This model is also called a “dense liquid foundation”. An alternative approach utilises the elastic solid model, in which the applied load produces a continuous deformation. Granular and fine-grained unbound soils with lower shear strength are more similar to the dense liquid model, whilst bonded or stabilised materials exhibit more similarity to the elastic solid model.

In this paper the base is modelled as a structural solid layer interacting with the slab and the rest of the foundation (the granular subbase & the subgrade) characterised by a single *k*-value (Fig. 5(b)). The *k*-value in the model acts as linear compression only vertical springs. The interface between the concrete slab and the base (Fig. 5(c)) is modelled by the surface-based contact formulation in ABAQUS (2010). In this manner, it is possible to take into account the relative movement between the slab and the base (e.g. frictional behaviour, up-lift and loss of support due to curling). The finite-sliding approach is chosen to allow for arbitrary relative separation, sliding, and rotation of the contacting surfaces. The friction stress is related to the contact pressure through the concept of Coulomb friction model by assuming an isotropic friction coefficient of $\mu$=0.5 (based on BS EN 12812 (2008)) and a maximum of 100 kPa friction stress (McCullough and Rasmussen 1998). There is no bond between the concrete slab and the foundation and only the self-weight of the slab resists up-lift, as is expected in most practical cases (Channakeshava et al. 1993).

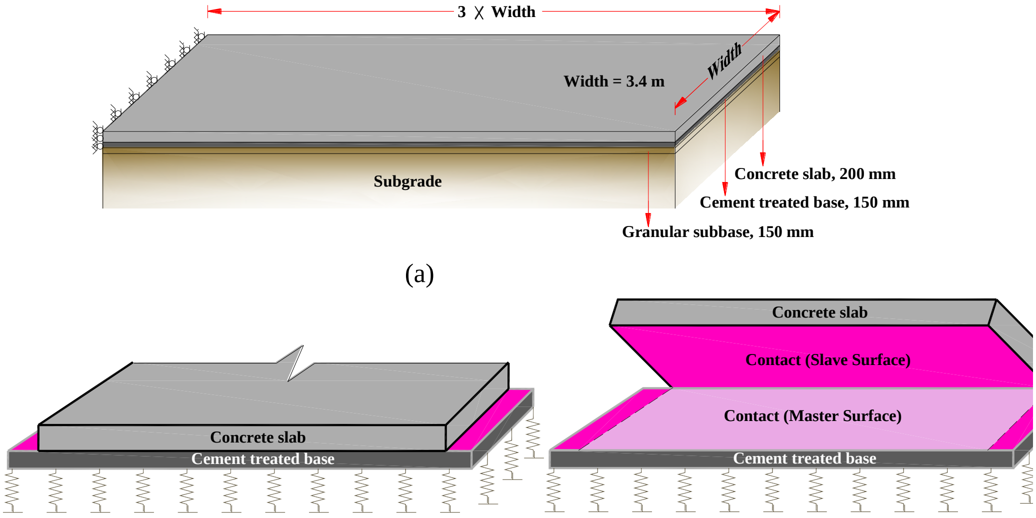

(a)

(b) (c)

**Fig 5** (a) Continuity of the pavement in modelling; (b) Modelling of the foundation layers; (c) Contact surfaces

The base layer is considered as an isotropic, homogeneous and linear elastic material. A moderate *k* value of 0.04 N/mm$^3$ is used for the subgrade soil. This value is increased by 50% to account for the effect of the thin layer of granular material used to improve the stiffness of the soil, thus the modulus of reaction at the top of the subbase is assumed to be 0.06 N/mm$^3$. The cement bound base is considered to have a thickness of 150 mm with a long-term elastic modulus of 8 GPa, and a Poisson's ratio of 0.3.

### *3.1.4 Drying creep*

Since tensile stresses are dominant in the design of concrete pavements, the term "creep" in this paper refers to tensile creep. Drying creep has two components; "intrinsic" creep, and "microcracking" as an apparent component of creep (Altoubat and Lange 2003). Intrinsic creep mainly occurs during the elastic (pre-cracking) stage, since in the post-cracking stage tensile stresses are released by crack opening. In this analysis, the "microcracking" component of drying creep is automatically taken into account, since the smeared cracking model is used. Nonetheless, the intrinsic component of drying creep is ignored. This seems reasonable when trying to identify the highly distressed zones on the surface, since the tensile strain sustained by concrete during the elastic phase is relatively small compared to the strain developed in the post-cracking phase.

### *3.1.5 Maturity*

Maturity of concrete is accounted for by using equations given in BS EN 1992-1-1 (2004) with the value of s=0.38 (a experimentally obtained coefficient which depends on the type of cement). The "hygral contraction coefficient" is not considered to be affected by maturity, in the same way as for the thermal coefficient of expansion (ACI 209R 1992).

## 3.2 Moisture transport and shrinkage analysis

In the analysis, the concrete slab can adjust dynamically its moisture relative to the environment. The top surface of the slab is exposed to a constant ambient humidity of 40% and other surfaces are assumed to be sealed with no moisture interaction with the neighbouring domains. The relative humidity of 40% is a medium to low value for outdoor conditions. Lower environmental relative humidity accelerates drying shrinkage and higher values may delay it. Initially, the concrete moisture content is set equal to 1.0 (saturation condition).

For moisture movement analysis, the heat transport module of ABAQUS is used. Free moisture content is replaced by temperature, and moisture diffusivity by thermal conductivity. To avoid the effect of extra multipliers needed in the heat transfer equation but not in the moisture transport equation, specific heat and density is taken equal to unity. This analysis is then coupled with structural analysis to calculate shrinkage deformations. For this purpose, hygral contraction coefficient is replaced by thermal coefficient of expansion.

ABAQUS 8-noded fully integrated solid elements are used; element type DC3D8 for moisture transport analysis and C3D8 for stress analysis. The optimum element size through the thickness was chosen to be 25 mm, based on a mesh sensitivity study in moisture transport analysis (Jafarifar 2012). The optimum horizontal dimension of 120 mm was also chosen for elements from a mesh sensitivity in stress analysis (Jafarifar 2012).

### *3.2.1 Moisture transport*

The numerically calculated time history of moisture profiles is presented in Fig. 6(a) for a period of 1 year. Fig. 6(b) shows the moisture contours after the 1 year of drying. It can be seen that the penetration of drying into the depth occurs at a very slow rate, e.g. after one year of drying, the moisture content only reaches 63% at a depth of 25 mm from the drying surface. The results of the moisture transport analysis are used in the next section to obtain the time history of shrinkage strains.

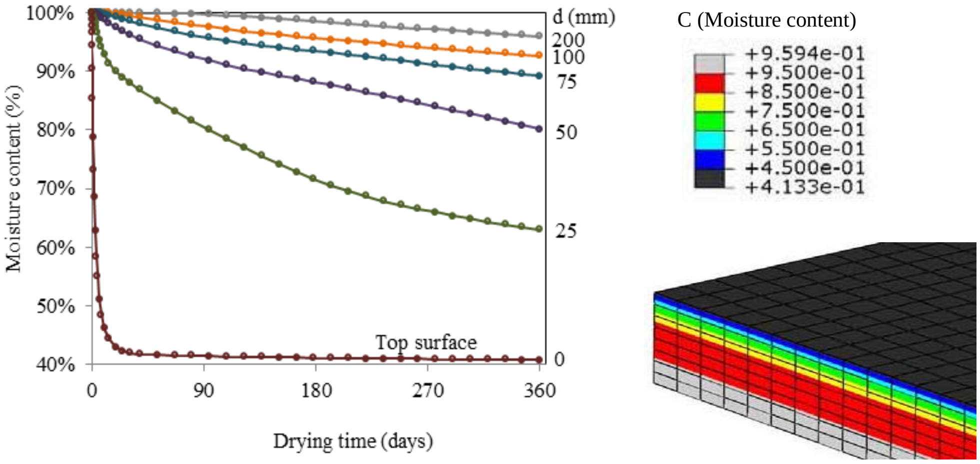

(a) (b)

**Fig 6** (a) Time history of moisture variation through the depth; (b) Moisture content contour after 1 year of drying

### *3.2.2 Shrinkage analysis*

The results show that the pavement curls upwards due to drying shrinkage (see Fig. 7). Contact opening under the slab occurs over a large area, and only a small fraction of the contact surface remains in touch to transfer the slab weight to the foundation.

In damage plasticity the inelastic strain, IE (also called cracking strain), can be interpreted as crack width over the element length, based on its definition. The orientation of cracking strains, indicating the direction of crack openings, is shown in Fig. 7(a). The cracking strain contours after one year of drying at the top surface and at 25, 50 and 75 mm depths are shown in Fig. 7(b) to (e), respectively. A nearly uniform cracking strain can be seen in the middle of the slab (along the length) decreasing towards the transversal free (uplifting) edge.

Based on reported field studies on conventionally reinforced slabs, shrinkage initially causes short and tiny micro-cracks which are shallow in depth and closely spaced (CORD 1992). Although the summation of these micro-crack openings over a unit length is considerable, each individual micro-crack is rarely visible to the naked eye. From Fig. 7(a), it can be deduced that the primary cracks include: (1) transversal surface cracks formed all over the slab (with lower density near the transversal edge); (2) diagonal surface cracks near the corner; and (3) longitudinal surface cracks near the middle of the transversal edge.

After one year of drying, the short-spaced transversal micro-cracks at the middle part of the slab have an average opening density of 0.69 mm/m at the top surface (Fig. 7(b)), which decreases to 0.5 mm/m at a depth of 25 mm (Fig. 7(c)) and 0.19 mm/m at a depth of 50mm from the surface (Fig. 7(d)). These cracking strains diminish gradually at greater depths (Fig. 7(e)).

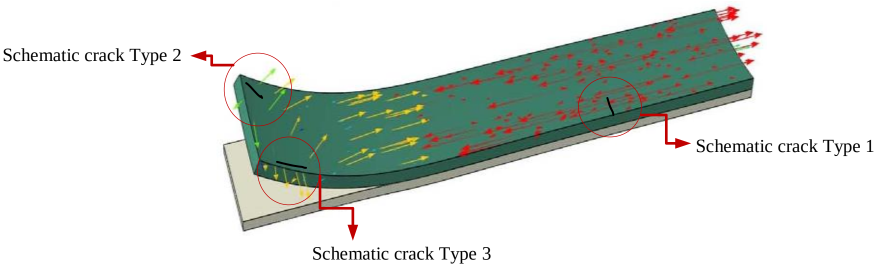

(a) Orientation of cracking strains

(b) Strain contour for the top surface

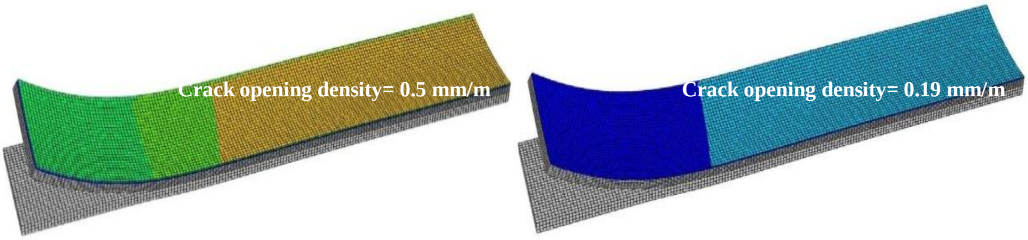

(c) Strain contour at 25 mm depth (d) Strain contour at 50 mm depth

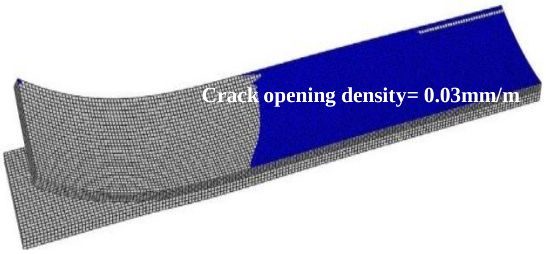

(e) Strain contour at 75 mm depth

**Fig 7** Maximum principal component of inelastic (cracking) strains due to shrinkage after one year of drying (half width of the pavement is shown)

Fig. 8 shows the time history of the maximum cracking strain at the top surface and at the depths of 37.5 and 62.5 mm of the slab. It can be seen that cracking at the top surface initiates from the beginning of drying, whilst at a depth of 37.5 mm this occurs after 7 days of drying. The crack penetration reaches a depth of 62.5 mm after 225 days of drying. It is also observed that the cracking strain at the top surface approaches a constant value after about 180 days of drying. This means that the crack width on the surface due to shrinkage stabilises after a certain period of time.

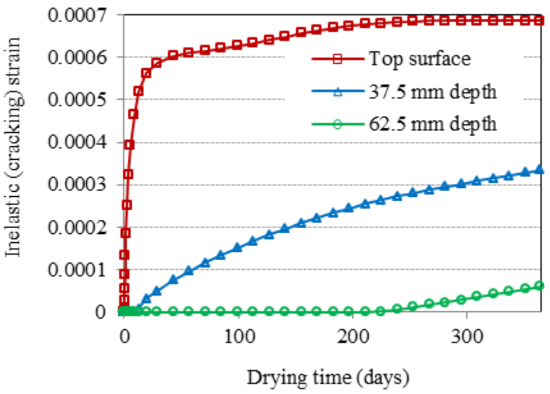

**Fig 8** Time history of maximum cracking strains at various depths

Fig. 9 shows the time history of the corresponding maximum tensile stress (left hand axis) at the same depths as those in Fig. 8. Although the maximum crack opening occurs on the top surface, the maximum tensile stress is not developed at that location. As shown in Fig. 9, the maximum tensile stress at the top surface is significantly smaller than that at a depth of 37.5 mm. This is because shrinkage cracking at the top surface occurs at a very early age, when the concrete strength is still low. At the depth of 37.5 mm, shrinkage cracking initiates after 7 days (see Fig. 8) when the strength of the concrete is much higher. Therefore, a higher tensile stress is resisted by the concrete slab at that depth. The maximum tensile stress was recorded at the depth of 62.5 mm, since the drying front reaches that depth when the concrete is well matured. It should be noted that, at the bottom of the slab compressive stresses are developed to balance the stress demand through the section.

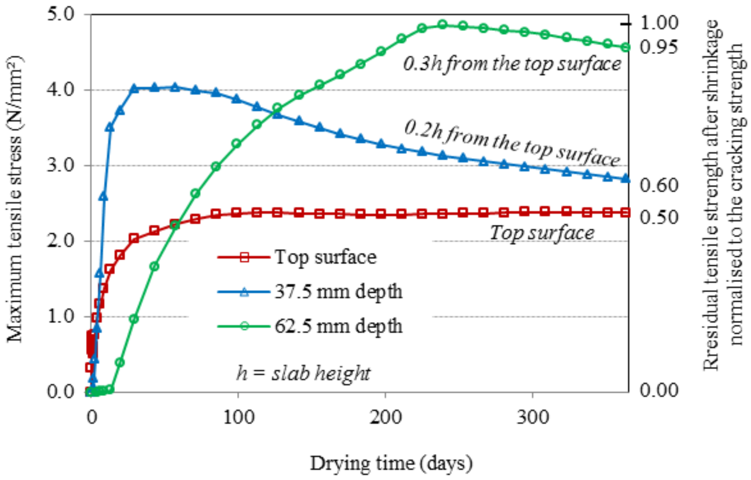

**Fig 9** (a) Left axis: Time history of maximum tensile stresses at various depths; (b) Right axis: Residual tensile strength after shrinkage, normalised to the cracking strength (4.8MPa)

### *3.2.3 Crack width and spacing*

Bazant et al. (1979 and 1982) predicted a system of parallel cracks with initial spacing $S_0$, in a homogenous concrete domain due to non-uniform shrinkage. In this prediction with further penetration of the drying front, secondary and tertiary cracks with spacing $2S_0$ and $4S_0$ are formed and some of the initially formed cracks close. Formation of primary, secondary and tertiary microcracks due to differential shrinkage was confirmed later on by a numerical study performed by Granger (1997). Using the Bazant et al. (1979 and 1982) approach and assuming a lower bound of crack spacing (e.g. $S_0$ in order of the maximum aggregate size, 14 mm), the cracking density obtained in Fig. 7(b) can be transformed into crack spacing in the range of 14 -56 mm with an opening in the range of 0.01-0.04 mm at the stabilised state of drying.

### *3.2.4 Comparison of FEA results with Concrete Society TR34 design method*

The residual tensile strength of the R-SFR-RCC slab after shrinkage (365 days) is normalised with the cracking strength of mature concrete (see Fig. 9 (right hand axis)). It can be seen that the residual strength on the top surface stabilises at around 50% of the maximum tensile strength of mature concrete. This ratio reaches 60% at the depth of 37.5 mm (0.2*h*) and 95% at the depth of 62.5 mm (0.3*h*).

Concrete Society TR34 (2003) gives a detail design procedure for SFRC slabs on grade. It is not exactly the case for SFRC roads, but is the only guideline that uses flexural characteristics. This guideline concedes that the interaction between shrinkage stresses and loading in concrete ground-slabs is not well understood. However, it advises to account for shrinkage particularly when significant negative moments (hogging) could occur due to imposed loads. Examples are given on how to evaluate shrinkage stresses induced by external and internal (curling) restraints using simple calculations. The guideline then uses the average value of these stresses to reduce the flexural tensile strength of concrete when calculating the negative moment capacity of the uncracked cross section.

Using TR34 to take into account shrinkage, for the R-SFR-RCC pavement examined herein, the tensile flexural strength must be reduced by 25-35% (average 30%) as shown in Fig. 10(a). Based on the FEA results presented in Fig. 9 (right hand axis) the actual loss of strength due to drying shrinkage is 50% at the top surface but reduces quickly to zero. This is shown in Fig. 10(b) in comparison to the reduction assumed by TR34; it is clear that the tensile capacity at the top surface is reduced more than that predicted by TR34 while the concrete below the surface is much less affected by shrinkage.

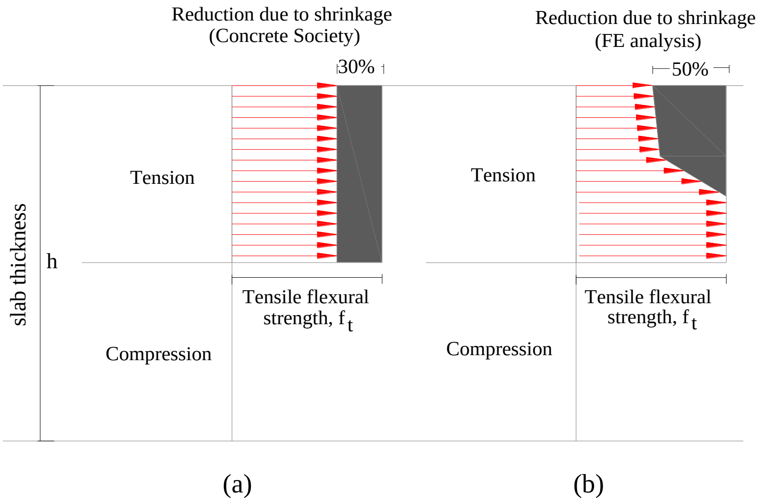

**Fig 10** Negative moment capacity; (a) Reduction due to shrinkage based on TR34; (b) Reduction due to shrinkage based on the FEA results presented in Fig. 7

For pavements, this study shows that the stress induced by the effect of internal restraint (or curling) is dominant over that induced by friction. This is because differential shrinkage causes the curled slab to move upwards and hence no external restraint is mobilised due to separation for a large part of the contact area.

## 3.3 Stress analysis of the pavement under monotonic loading

Two conditions were examined: (1) monotonic wheel load only; (2) monotonic wheel load after shrinkage in the first year. For both conditions, the load carrying capacity is evaluated for different levels of damage based on crack initiation, opening and penetration. Since the analyses are performed in a comparative manner, load safety factors are not needed and are not used.

### *3.3.1 Monotonic loading only*

Four load configurations are considered, as shown in Fig. 11. For corner loading and longitudinal edge loading, one end of the axle is located on the slab (assuming that the other end is on the adjacent segment separated by the longitudinal joint).

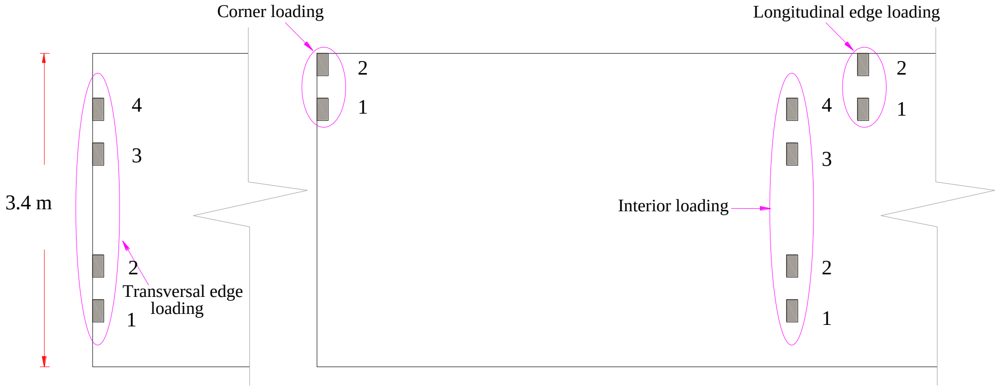

**Fig 11** Configurations assumed for corner, edge and interior loading

Under the corner load for condition 1 (without shrinkage), Fig. 12(a) shows the inelastic (cracking) strain versus axle load (bottom axis) and normalized axle load (top axis) for three damage levels defined in the diagram. As shown in this figure, the slab behaves elastically until the axle load reaches 4.2SAL, then cracking initiates under tyre 1 at the bottom surface. At the top surface, corner cracking initiates due to negative moment, when the axle load reaches 5SAL. This crack penetrates to half of the slab depth when the axle load reaches 8SAL. Fig. 12(b) shows the contour of cracking strains, at 8SAL; in this diagram diagonal distribution of peak strains indicates a corner break. Fig. 12(c) shows the profile of the maximum cracking strain at the top surface versus a diagonal distance from the corner, "*w*", for various loads. Assuming that crack opening localises at the region of maximum cracking strain, the area under each curve represents "the equivalent crack opening". Fig. 12(d) shows the variation of "the equivalent crack opening" versus the axle load. For this condition, which ignores shrinkage and fatigue, the equivalent opening of the corner crack exceeds 0.5 mm when the axle load exceeds 9.5SAL.

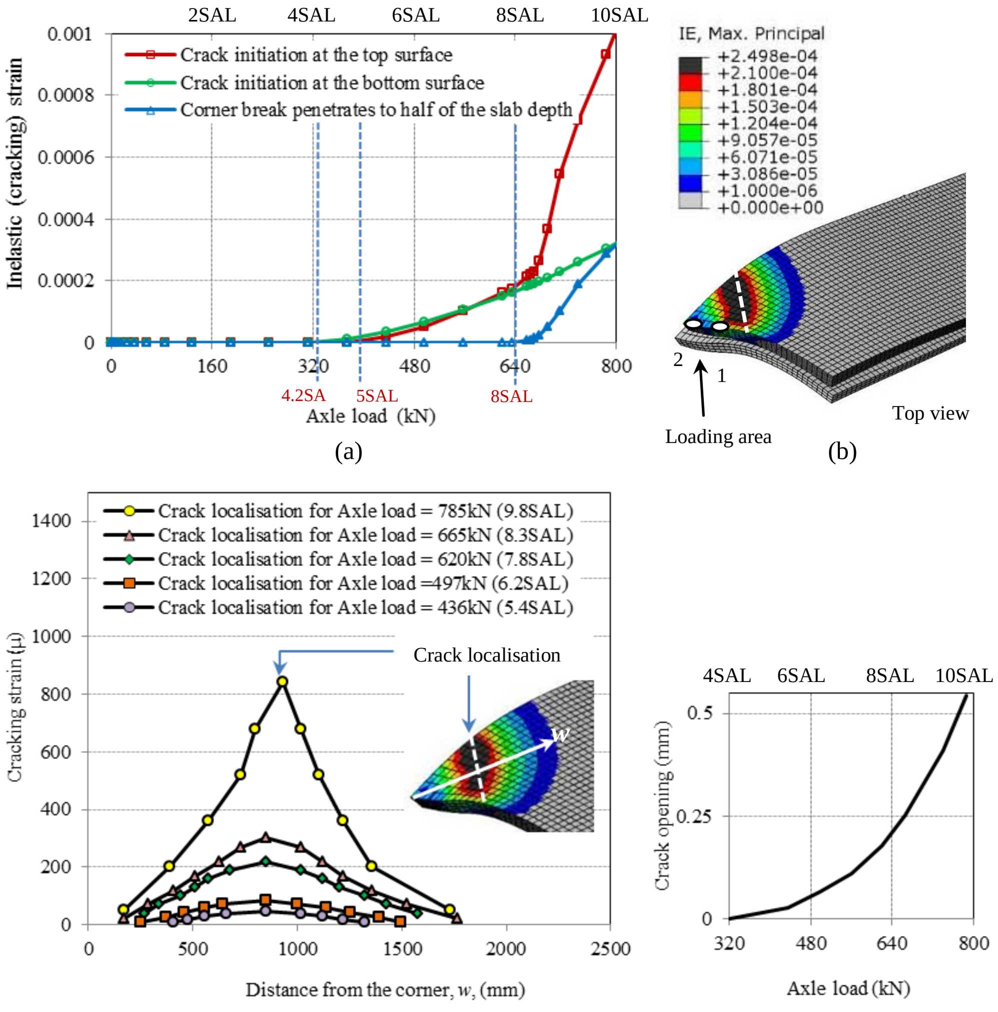

(a)

(b)

(c)

(d)

**Fig. 12** Corner load only (a) Cracking strain versus axle load; (b) Maximum cracking strain under one end of an axle load = 8SAL; (c) Maximum cracking strain at the top surface versus the distance from the corner; (d) Variation of "the equivalent crack opening" versus axle load

Following the same approach, comparative analysis was carried out for the other load configurations shown in Fig. 11. The summary of the results is given in Table 1 in terms of the load bearing capacity for various damage levels and is discussed in Section 3.3.3.

| | Load cases | | | |
|---|---|---|---|---|
| Damage level | Corner load only | Longitudinal edge load only | Transversal edge load only | Interior load Only |
| Crack initiation at the bottom surface | 340 kN<br>(4.25SAL) | 280 kN<br>(3.5SAL) | 465 kN<br>(5.8SAL) | 440 kN<br>(5.5SAL) |
| Crack initiation at the top surface | 400 kN<br>(5SAL) | 650 kN<br>(8.15SAL) | 585 kN<br>(7.3SAL) | > 1600 kN<br>(>20SAL) |
| Top cracking reaches half of the slab depth | 640 kN<br>(8SAL) | 1200 kN<br>(15SAL) | 960 kN<br>(12.0SAL) | > 1600 kN<br>(>20SAL) |
| Bottom cracking reaches half of the slab depth | - | 530 kN<br>(6.6SAL) | 835 kN<br>(10.4SAL) | 745 kN<br>(9.3SAL) |
| | Corner load + shrinkage | Longitudinal edge load + shrinkage | Transversal edge load + shrinkage | Interior load + shrinkage |
| Crack initiation at the bottom surface | 95 kN<br>(1.2SAL) | 400 kN<br>(5SAL) | 400 kN<br>(5SAL) | 590 kN<br>(7.4SAL) |
| Crack widening at the top surface | 80 kN<br>(1SAL) | 25 kN<br>(0.3SAL) | 40 kN<br>(0.5SAL) | 25 kN<br>(0.3SAL) |
| Top cracking reaches half of the slab depth | 320 kN<br>(4SAL) | 620 kN<br>(7.75SAL) | 520 kN<br>(6.5SAL) | 1500 kN<br>(18.75SAL) |
| Bottom cracking reaches half of the slab depth | - | 720 kN<br>(9SAL) | 880 kN<br>(11SAL) | 1000 kN<br>(12.5SAL) |

Table 1 Load bearing capacities for various load cases and damage levels

### *3.3.2 Monotonic loading after restrained shrinkage*

For condition 2 (with shrinkage), the pavement initially curls upward due to non-uniform shrinkage and micro-cracks develop all over the slab surface (see Section 3.2). The monotonic corner loading is then applied and increased until collapse. Fig. 13(a) shows that no significant increase in the cracking strains occurs on the top surface when the load is less than 1SAL. When the axle load exceeds 1SAL, cracking strains at the top surface start increasing and that signifies the initiation of the corner break. The (concentrated) corner crack penetrates to half of the slab depth when the load reaches 4SAL. Fig. 13(b) shows the max principal cracking strains at 4SAL. Fig. 13(c) shows the profile of the maximum cracking strain on the top surface versus distance, "*w*", from the corner for various axle loads. The area under these curves represents "the equivalent crack opening" over and above any initial micro-cracking distributed with a spacing of 56 mm (as estimated in Section 3.2.3). As shown in Fig. 13(c), at the corner area of the slab a value of 450 micro-strain is developed due to drying shrinkage prior to applying the load, forming distributed micro-cracks. When the load is applied, the micro-cracks initially widen and no significant localisation occurs until the load reaches 2.5SAL. For larger loads, the cracking strain is localised at a specific distance from the corner as seen in Fig. 13(c) and 13(d).

Fig. 13(d) shows “the equivalent crack opening” versus the load, with and without shrinkage. This comparison shows that distress induced by drying shrinkage at the top surface significantly increases the crack opening developed due to loading, though shrinkage does not initially induce visible cracks. For example the corner crack opening of 0.5 mm, which corresponded to 9.6SAL in the case of corner load only, increases to 1.0 mm when drying shrinkage is considered. At 6.8SAL the crack width increases 500% if shrinkage is taken into account.

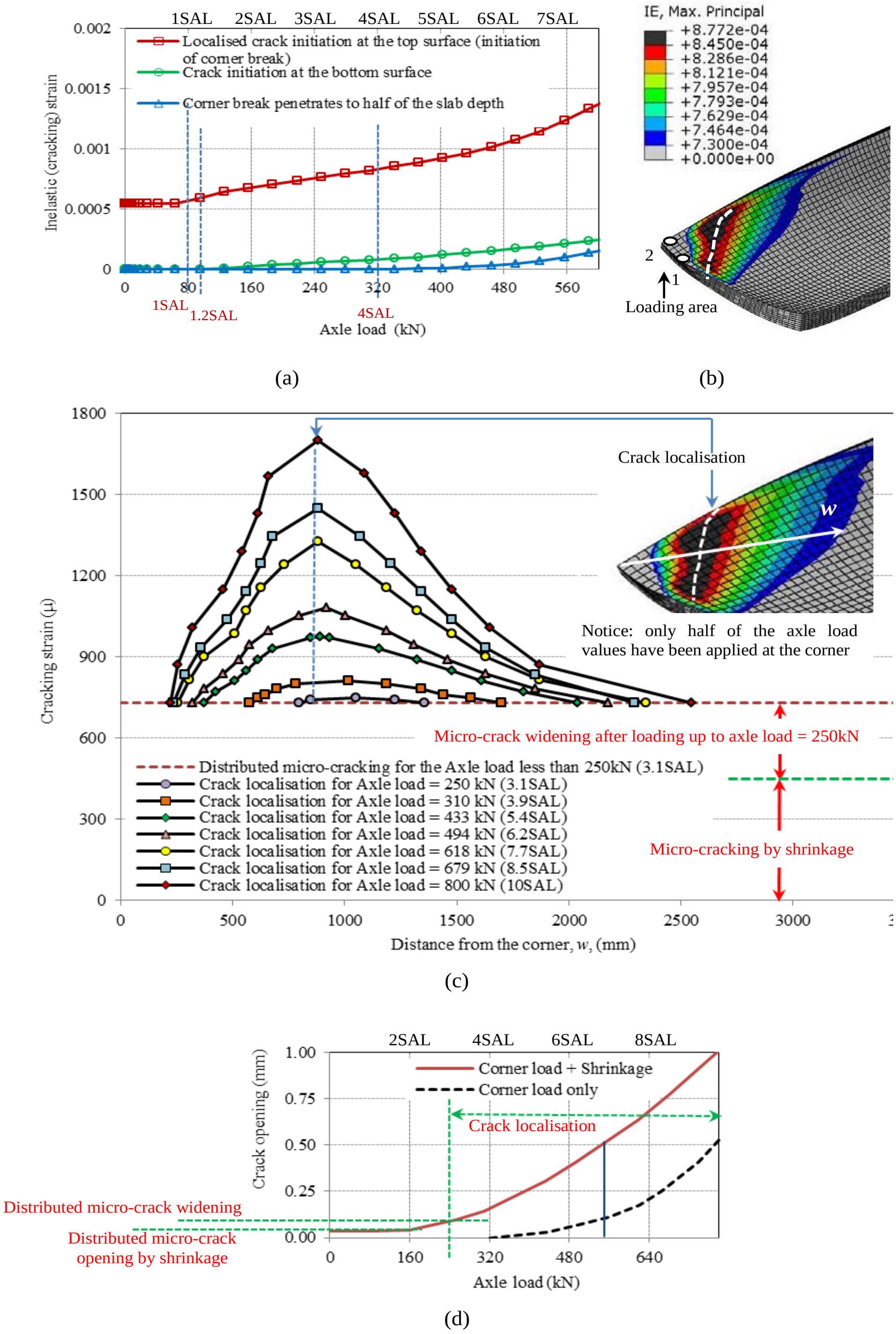

(a)

(b)

(c)

(d)

**Fig. 13** Corner load + Drying shrinkage (a) Cracking strain versus axle load; (b) Maximum cracking strain under one end of an axle load = 4SAL; (c) Maximum cracking strain at the top surface versus the distance from the corner; (d) Variation of “the equivalent crack opening” versus axle load

The same approach was followed for the other load configurations and the summary of the results is given in Table 1 and is discussed next.

### 3.3.3 Discussion

To evaluate the load carrying capacity of pavements, a criterion representing “end of life” or “failure” is required. For ultimate limit state, the collapse condition controls the load carrying capacity. For serviceability limit state, the pavement must remain functional with an acceptable level of damage, for example the crack width must be kept below a specified amount (e.g. 0.5 mm to prevent loss of aggregate interlock and damage due to water penetration (Hassan et al. 2005)). Owners and designers of slabs are often more concerned about the obvious serviceability limit state of cracking at the top surface rather than the ultimate limit state. However, in most practical cases, surface cracking also depends on the finish materials (Eyre 2006). Therefore, “end of life” criteria are sometimes descriptive and the choice is left to the designer.

Top-surface crack initiation (as specified by TR34) is not an ideal limit state since it ignores shrinkage distress. Penetration of the top surface crack to the bottom is also inadequate as a failure criterion, since the corresponding failure load is extremely high (due to stiff reaction of the pavement and the cement treated base). As a result, a more moderate failure criterion is adopted in this study based on the penetration of top surface cracking to half of the slab depth.

Top surface cracking is dominant in the case of corner loading. The results presented in Table 1 show that the “failure” load when shrinkage is ignored is twice than that of the condition when shrinkage is considered for corner and edge loading.

In the case of interior loading, bottom surface cracking is dominant. Shrinkage pre-stresses the slab and puts the bottom surface under compression before the load application. Hence, at the bottom of the slab, the cracking capacity for interior loading plus shrinkage is higher than when ignoring shrinkage (the same applies for longitudinal edge loading).

# 4 Long-term fatigue analysis

Long-term fatigue analysis was performed to investigate the effect of initial distress due to shrinkage on the fatigue performance of SFRC pavements. Fatigue test data obtained by Graeff et al. (2012) for the Ecolanes project are used for this purpose.

Traditionally, the number of cycles until initial cracking from beam tests is used to represent the concrete’s fatigue life for a given stress ratio. Nonetheless, for indeterminate structures such as ground-supported slabs, the first crack does not necessarily represent the end of fatigue life (Roesler et al. 2005). In the case of SFRC, where higher loading capacity can be utilized in the post-cracking phase, relying directly on the results of beam fatigue tests may be misleading (Altoubat et al. 2008). Analytically, the main factor causing differences in the fatigue behaviour of concrete slabs and beams is the definition of failure. Concrete ground slabs have a higher fatigue life than predicted by beam fatigue equations due to the differences in defining the stress ratio in beams and slabs (Roesler 1998).

Roesler et al. (2005) found that if the ultimate flexural strength of a slab could be measured and replaced by the modulus of rupture (MOR) of a beam in the fatigue equation, then the fatigue behaviour of a slab can be predicted using that equation. Therefore, to accurately predict the fatigue life of a concrete slab, the flexural strength of the slab must be known. The flexural strength of a slab depends on many factors (such as the thickness and geometry of the slab, boundary conditions and loading configuration) and a monotonic test is usually required to obtain it. In the absence of cost prohibitive physical testing, in the current study, the numerically obtained monotonic flexural strength of the slab is utilised.

For the R-SFR-RCC mix adopted in the current research, the fatigue endurance curve for beams obtained by Graeff et al. (2012) is used, as given in Eq. 2.

$$\log(N) = -15S + 15 \quad \text{(Eq. 2)}$$
$$R^2 = 0.71$$

Where, $N$ is the number of cycles to failure; $S$ is the stress ratio; and $R^2$ is the linear regression coefficient.

Studies show that the fatigue life of pavements is usually controlled by the few axles passing along the slab edge (Jiang and Tayabji 1998; Huang 2004). To correlate the fatigue life at the pavement edges to the interior areas, the distribution of load placement across the traffic lane must be known theoretically. The Portland Cement Association (PCA 1984) studied this issue and found that the same fatigue damage can be obtained by considering edge loading only and assuming 6% of the total number of cycles being applied at the edge of the pavement. Hence, for 300 msa, the pavement should be able to pass 18 msa through the edges during its service life.

## 4.1 Safety margins

Using the fatigue endurance curve (Eq. 2), the pavement stress ratios are calculated for the design load cycles as given in Table 2. Assuming an 80 kN standard axle as the service load, the minimum required load bearing capacities are calculated for interior areas and edges (see Table 2). Safety margins are shown in Table 2 with and without considering shrinkage. It can be seen that the minimum safety margin of 2.1 is given when considering shrinkage distress. The safety margin when shrinkage is ignored increases to 4.1. This shows that the fatigue capacity of pavements could be overestimated by around 100%, if shrinkage distress is ignored.

| | Corner load | Longitudinal edge load | Transversal edge load | Interior load |
|---|---|---|---|---|
| Designed number of cycles | 18 msa | 18 msa | 300 msa | 300 msa |
| Stress ratio based on the endurance curve | 0.516 | 0.516 | 0.434 | 0.434 |
| Service load (Axle* Load, kN) | 80 | 80 | 80 | 80 |
| Minimum required load bearing capacity based on the stress ratio (Axle* Load, kN) | 155 | 155 | 184 | 184 |
| Ignoring shrinkage distress | | | | |
| Failure load based on FE analysis (Axle* load, kN) | 640 | 1,200 | 960 | 1,850 |
| Safety margin | 4.1 | 7.7 | 5.2 | 10.0 |
| Considering shrinkage distress | | | | |
| Failure load based on FE analysis (Axle* load, kN) | 320 | 620 | 520 | 1,500 |
| Safety margin | 2.1 | 4.0 | 2.8 | 8.1 |

*only half of the axle load is applied at the edge and corner

Table 2 Provided safety margins in the long-term

## 4.2 Allowable stress ratios

To deal with fatigue in another way, the reduction in the allowable stress ratio due to shrinkage distress is examined. From the experimental fatigue endurance curve (Eq. 2), for 300 msa the allowable stress ratio is 0.435; and for 18 msa the allowable stress ratio is 0.516. By considering shrinkage distress the permitted stress ratios should also be reduced, depending on the reduction in the failure loads.

The monotonic failure load (MOR) when considering shrinkage distress is reduced, as shown in Table 3 (failure defined as top cracks propagating to half of the slab depth). If this reduction is applied in the experimental fatigue endurance curve, the relation between the stress ratio and the allowable number of load cycles changes as shown in Fig. 14. This figure also shows that considering shrinkage distress, to pass 300 msa, the stress ratio should be reduced from 0.435 to 0.352 for the interior areas and to 0.235 for the transversal edges (the transversal edge being dominant). To pass 18 msa (6% of the total number of cycles) the stress ratio should also be reduced from 0.516 to 0.266 in the longitudinal edges and to 0.258 in corners (corner is dominant). Therefore, for shrinkage the allowable stress ratio of the pavement should be reduced by around 50%. This agrees completely with the results of Section 4.1.

| Load configuration | Corner loading | Longitudinal edge loading | Transversal edge loading | Interior loading |
|---|---|---|---|---|
| Failure load reduction factor | 0.50 | 0.52 | 0.54 | 0.8 |

Table 3 Failure load reduction factors when shrinkage distress is considered

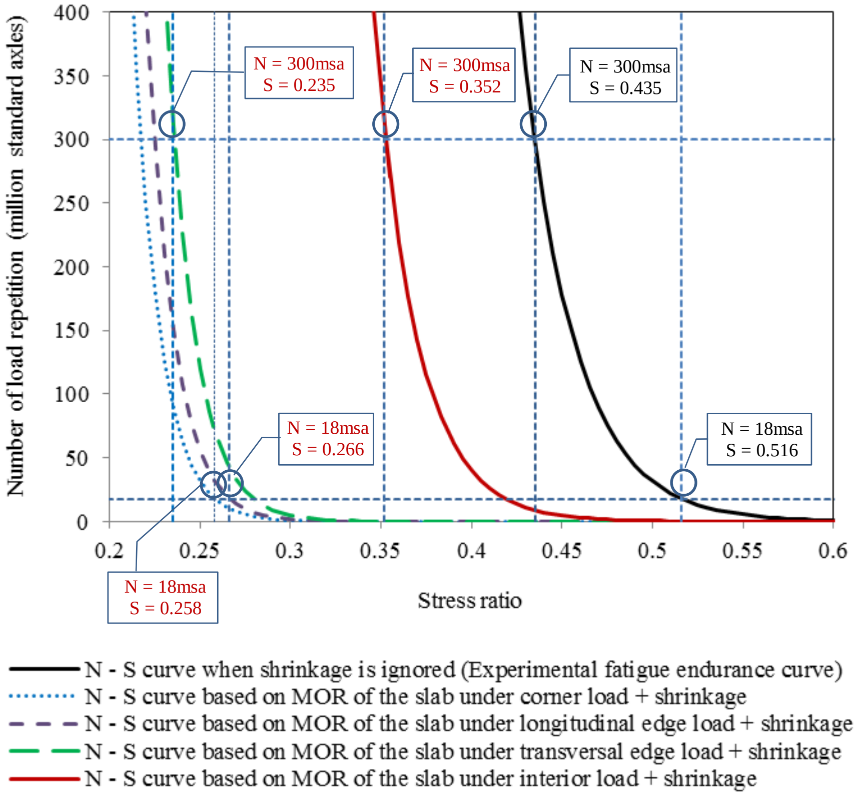

**Fig. 14** Comparison of N-S curves when shrinkage distress is considered or ignored

# 5 Verification

This study coupled several aspects of concrete pavement behaviour, including: (1) moisture transport mechanisms during drying; (2) shrinkage induced damage; (3) long-term fatigue performance. To validate such a study overall, field studies or laboratory tests considering the above aspects together are needed which were not found in the literature. Alternatively, the individual components of this study have been verified separately and compared with data available in the literature.

The model developed for moisture transport analysis was validated against results from the research carried out by Asad et al. (1997). The geometry and the boundary conditions of the experimental samples are illustrated in Figure 15(a). The comparison between the results of the experimental and analytical work carried out by Asad et al. (1997) with the model developed in the current paper shows good agreement (see Figure 15(b)).

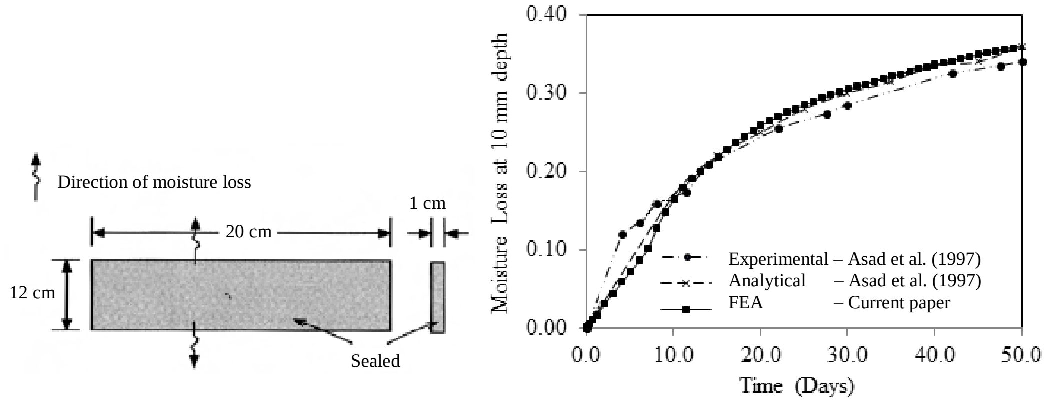

(a) (b)

**Fig. 15** (a) Experimental moisture transport samples (Asadet al. 1997); (b) Verifying the results of the model developed for moisture transport in the current paper against Asad et al. (1997)

The performance of the model pavement under traffic load was verified using the closed-form equations of Westergaard in the elastic range and Meyerhof elasto-plastic theory in the ultimate limit state, as also suggested by Concrete Society TR34 (2003)). A comparison of the load bearing capacity with the Concrete Society TR34 (2003) method is given in Table 4. These values predict the maximum load bearing capacity without considering the effect of shrinkage or fatigue. Despite the simplifications in the closed-form equations (such as concentrating the loads in circular shapes, etc.), the two predictions match well. By applying the partial safety factors provided in TR34, the load bearing capacity, which is controlled by the corner loading, reduces from 6 to 2.5 SAL.

| | | Failure criterion : crack initiation at the top surface ** | | |
|---|---|---|---|---|
| | | Current study | Concrete Society TR34 method | |
| | | Ultimate load bearing capacity | Ultimate load bearing capacity | With partial safety factc |
| Axle* Load (kN) | Interior | >1600 (>20SAL) | 1390 (17.4SAL) | 579 (7.2SAL) |
| | Edge | 650 (8.15SAL) | 695 (8.7SAL) | 290 (3.6SAL) |
| | Corner | 400 (5SAL) | 475 (6SAL) | 199 (2.5SAL) |

*only half of the axle load is applied at the edge and corner

**without considering the effect of shrinkage

Table 4 Load bearing capacity of the SFR-RCC Pavement (for model verification; comparison with TR34)

The overall predicted behaviour of the model pavement also matches field study observations. For example, it has been reported that differential shrinkage produces increased slab stresses and deformations under loads (NCHRP Report 372 1995); the early age stresses may immediately cause cracking or remain as residual stresses limiting the capacity of concrete and influencing its fatigue life (Altoubat and Lange 2001; Ruiz et al. 2005). Initially invisible microcracks get longer and wider to form a visible crack over time (Ruiz et al. 2005). Top-down corner break (Ruiz et al. 2005) or edge cracking (ACI 544.4R 1999) is the mode of failure for partially supported upward curled slabs.

# 6 Conclusion and summary

A methodology has been developed for studying the restrained shrinkage behaviour of SFRC pavements by using finite element analysis and utilising material properties from experiments. For typical RCC pavements incorporating recycled fibres, the results show that:

- Before traffic loading, shrinkage causes curling which results in slab uplift and loss of contact with the ground. A nearly uniform cracking strain is produced along the length of the slab decreasing towards the transversal free edge.
- Though shrinkage does not initially produce visible cracks, distress induced by drying shrinkage significantly increases crack opening development due to loading (up to 500% for a crack width of 0.5 mm).
- Due to shrinkage, the tensile strength at the top surface can reduce by around 50%. This strength loss mainly occurs in the top quarter of the slab depth. Tensile stresses at the top, induced by shrinkage, also result in compressive stresses at the bottom of the slab (reducing tensile stresses at the bottom arising by traffic load in the interior areas of the slab, by around 30%).
- The overall load bearing capacity of SFRC pavements can be overestimated by twice if shrinkage distress is ignored, both in short-term and when fatigue loading is included.

This study focused on a specific type of concrete pavement and utilised typical environmental and boundary conditions, though the developed methodology can be used for any concrete type, slab geometries and boundary conditions. The relative humidity of 40% assumed in this study is a medium to low value for outdoor conditions. Lower environmental relative humidity accelerates drying shrinkage and higher values may delay it.

## Acknowledgment

The authors acknowledge the financial support of the 6th Framework Programme of the European Community under contract number 031530.

## References

ABAQUS Version 6.10 (2010) Dassault Systèmes Simulia Corp., USA.
ACI 209R (1992) Prediction of creep, shrinkage, and temperature effects in concrete structures. Amer Concr Inst, USA.
ACI 544.1R (1996) State-of-the-art report on fibre-reinforced concrete. Amer Concr Inst, USA.
ACI 544.4R (1999) Design considerations for steel fibre reinforced concrete. Amer Concr Inst, USA.
Achilleos C., Hadjimitsis D., Neocleous K., Pilakoutas K., Neophytou P. and Kallis S. (2011) Proportioning of steel fibre reinforced concrete mixes for pavement construction and their impact on environment and cost. Sustainability 3 (7): 965-983.

Altoubat S.A., Roesler J.R., Lange D.A., Rieder K. (2008) Simplified method for concrete pavement design with discrete structural fibres. Constr Build Mater 22(3): 384-393.
Altoubat S.A., Lange D.A. (2003) A new look at tensile creep of fibre reinforced concrete. ACI Special Publications (216): 143-160.
Altoubat S.A., Lange D.A. (2001) Creep, shrinkage and cracking of restrained concrete at early age. ACI Mater J 98(4): 323–331.
Asad M., Baluch M.H., Al-Gadhib A.H. (1997) Drying shrinkage stresses in concrete patch repair systems. Mag of Concr Res 49(181): 283-293.
ASTM C 1018 (1997) Standard test method for flexural toughness and first-crack strength of fibre-reinforced concrete (using beam with third-point loading). Amer Standards, USA.
ASTM C 157 (2008) Test method for length change of hardened hydraulic cement mortar and concrete. Amer Stand, USA.
Bazant Z. P., Raftshol W. J. (1982) Effect of cracking in drying and shrinkage specimens. Cem and Concr Res 12: 209-226.
Bazant Z.P., Ohtsubo H. (1979) Stability and post-critical growth of a system of cooling or shrinkage cracks. International J of Fracture 15: 443-456.
Bazant Z.P., Najjar L.J. (1972) Nonlinear water diffusion in nonsaturated concrete. Mater & Struct 5(25): 3-20.
BS EN 12390-3 (2009) Testing of hardened concrete – Part 3: Compressive strength of test specimens. Br Stand Inst, London, UK.
BS EN 12617-4 (2000) Products and systems for the protection and repair of concrete structures-test methods - Part 4: Determination of shrinkage and expansion. Br Stand Inst. London, UK.
BS EN 12812 (2008) Falsework-performance requirements and general design. Br Stand Inst, London, UK.
BS EN 14651 (2005) Test method for metallic fibered concrete - Measuring the flexural tensile strength. Br Stand Inst, London, UK.
BS EN 1992-1-1 (2004) Eurocode 2: Design of concrete structures, Part 1-1: General rules and rules for buildings. Br Stand Inst, London, UK.
Casanova P., Rossi P. (1997) Analysis and design of steel fibre reinforced concrete beams. ACI Struct J 94 (5): 595 – 602.
Channakeshava C., Barzegar F., Voyiadjis G.Z. (1993) Nonlinear FE analysis of plain concrete pavements with doweled joints. J Transp Eng, ASCE 119(5): 763-781.
Concrete Society TR34 (2003) Concrete industrial ground floors; A guide to their design and construction. Technical Rep No. 34, UK.
CORD (1992) Catalogue of road defects. Highways Department: the Government of the Hong Kong Special Administrative Region, Publication No. RD/GN/015.
Embacher R.A., Snyder M.B. (2001) Life-cycle cost comparison of asphalt and concrete pavements on low-volume roads case study comparisons. Transp Res Rec 1749: 28-37.
Eyre J.R. (2006) Membrane action in ground-bearing concrete slabs. Proceeding of the Inst of Civil Eng, Struct & Buildings 159(SB3): 153-163.
Graeff A.G., Pilakoutas K., Neocleous K., Vania M. (2012) Fatigue resistance and cracking mechanism of concrete pavements reinforced with recycled steel fibres recovered from post-consumer tyres. Eng Struct 45: 385-395.
Granger L. (1997) Thoughts about drying shrinkage: Experimental results and quantification of structural drying creep. Mater & Struct 30: 588-598.
Hassan K.E., Chandler J.W.E., Harding H.M., Dudgeon R.P. (2005) New continuously reinforced concrete pavement designs. Highways Agency TRL Report TRL630, UK.
Huang Y.H (2004) Pavement analysis and design. University of Kentucky, ISEN 0-13-142473-4, Pearson Education.
Jafarifar N., Pilakoutas K., Bennett T. (2014) Moisture transport and drying shrinkage properties of steel-fibre-reinforced-concrete. Constr Build Mater 73 (2014) 41–50.
Jafarifar N. (2012) Shrinkage behaviour of steel-fibre-reinforced-concrete pavements. PhD thesis, University of Sheffield, UK.
JCI-S-003 (2007) Method of test for bending moment–curvature curve of fiber-reinforced cementitious composites. Japan Concr Inst.
Jiang Y.J., Tayabji S.D. (1998) Mechanistic evaluation of test data from long-term pavement performance jointed plain concrete pavement test sections. Transp Res Rec 1629: 32-40.
Kodikara J., Chakrabarti S. (2005) Modelling of moisture loss in cementitiously stabilised pavement materials. ASCE Int J Geomech 5(4): 295-303.
Kwon S.H., Shah S.P. (2008) Prediction of early-age cracking of fibre-reinforced concrete due to restrained shrinkage. ACI Mater J 105(4): 381-389.

Lee C.J., Lange D.A., Liu Y. (2010) Prediction of moisture curling of concrete slab. Mater & Struct 44 (4): 787-803.
McCullough B.F., Rasmussen R.O. (1998) Fast-track paving: concrete temperature control and traffic opening criteria for bonded concrete overlays, Volume I: Final Report. FHWA-RD-98-167, Office of Infrastructure R&D, Federal Highway Administration.
Nam J.H., Kim S.M., Won M.C. (2006) Measurement and analysis of early-age concrete strains and stresses: continuously reinforced concrete pavement under environmental loading. J Transp Res Board (1947): 79-90.
NCHRP Report 372 (1995) Support under portland cement concrete pavements. Transp Res Board, Washington, D.C.
Neocleous K., Angelakopoulos H., Pilakoutas K. and Guadagnini M. (2011) Fibre reinforced roller compacted concrete transport pavements. Transp 164 (TR2): 97-109.
Neocleous K., Pilakoutas K. and Tlemat H. (2006) Design issues of concrete reinforced with steel fibres recovered from tyres. ASCE J Mater in Civil Eng 18 (5): 677-685.
PCA (1984) Thickness design for concrete highway and street pavements. Portland Cement Association.
Pickett G. (1946) Shrinkage stresses in concrete. ACI J 17 (3): 165-204.
Rahman M.K., Baluch M.H., Al-Gadhib A.H. (1999) Modeling of shrinkage and creep stresses in concrete repair. ACI Mater J 96(5): 542-551.
RILEM TC 162 TDF (2002) Test and design method for steel fibre reinforced concrete-final recommendations: bending test. Mater & Struct 35(253): 579-582.
Roesler J.R., Hiller J.E., Littleton P.C. (2005) Large-scale airfield concrete slab fatigue tests. International J of Concr Pavements (IJCP) 1(1): 66-87.
Roesler J.R. (1998) Fatigue of concrete beams and slabs. PhD thesis, University of Illinois, Urbana, USA.
Rogers M. (2003) Highway engineering. ISBN 0-632-05993-1, Blackwell Publishing Ltd, Oxford.
Ruiz M., Rasmussen R.O., Chang G.K., Dick J.C., Nelson P.K. (2005) Computer-based guidelines for concrete pavements; Volume II: Design and construction guidelines and HIPERPAVE II user’s manual. FHWA-HRT-04-122, Federal Highw Administration, Austin, USA.
Sakata K. (1983) A study on moisture diffusion in drying and drying shrinkage of concrete. Cem and Concr Res 13(2): 216-224.
Selih J., Sousa A.C.M., Bremner T.W. (1996) Moisture transport in initially fully saturated concrete during drying. Transp in Porous Media 24: 81-106.
UoS (University of Sheffield) (2005) Thin wire reinforcement for concrete. Br Patent Application No 0130852.7 and 0511012.7, Sheffield, UK.
Zhang J., Li V.C. (2001) Influence of fibres on drying shrinkage of fibre-reinforced cementitious composite. J Eng Mech, ASCE 127(1): 37-44.